Modern Physics Letters B, Vol. 18, No. 25 (2004) 1275–1291

World Scientific
www.worldscientific.com

NEGATIVE REFRACTION AND SUBWAVELENGTH FOCUSING USING PHOTONIC CRYSTALS

EKMEL OZBAY

Department of Physics, Bilkent University Bilkent, Ankara 06800, Turkey
Nanotechnology Research Center, Bilkent, Ankara 06800, Turkey
ozbay@fen.bilkent.edu.tr

KAAN GUVEN*, ERTUGRUL CUBUKCU†, KORAY AYDIN* and B. KAMIL ALICI*

**Department of Physics, Bilkent University Bilkent, Ankara 06800, Turkey*
†*Faculty of Arts and Sciences, Harvard University, Cambridge, MA 02138, USA*

Received 4 November 2004

In this article, we present an experimental and numerical study of novel optical properties of two-dimensional dielectric photonic crystals (PCs) which exhibit negative refraction. We investigate two mechanisms which utilize the band structure of the PC to generate a negative effective index of refraction ($n_{\text{eff}} < 0$) and demonstrate the negative refraction experimentally. To the isotropic extend of n_{eff}, different PC slab structures are employed to focus the radiation of a point source. It is shown experimentally that the PC can generate an image of the source with subwavelength resolution in the vicinity of the PC interface. Using a different PC, one can also obtain a far field focusing. In the latter case, we explicitly show the flat lens behavior of the structure. These examples indicate that PC-based lenses can surpass limitations of conventional lenses and lead to novel optics applications.

Keywords: Photonic crystal; negative refraction; left-handed material.

1. Introduction

The rather uninteresting-sounding problem of the propagation of electromagnetic waves through periodically modulated dielectric or dielectric/metallic media turned out to be an enormously rich research subject in the last decade. These media are referred to as photonic crystals (PC) by the analogy of the photon to an electron moving in a periodic electric potential in a solid.[1] The periodicity gives rise to bands for the propagation of electromagnetic waves, and band gaps, where the propagation is prohibited for certain frequency range. The investigation of optical properties at the band-gap edges and of the cavity (defect) modes expanded rapidly into applications in photonic devices.[2] Using different materials (i.e. different

dielectric constants), and by adjusting the geometrical parameters of the crystal, the band structure, and hence the propagation of light can be modified virtually in any way in a controllable manner. Two advantages of PCs are worth mentioning here. First, the lack of confinement in a spatial direction does not hinder the investigation of essential features of the EM phenomena, hence one-dimensional (1D) or two-dimensional (2D) PC structures can be used in the first place, which are easier to fabricate compared to their 3D counterparts. Second, the flexibility in scaling the governing Maxwell's equations enables the study to be conducted in an appropriate range of the electromagnetic spectrum (e.g. microwave), before extending it to the intended regime (infrared or optical). Evidently, the enormous application possibilities in telecommunication and optical wavelength scale drive the fabrication of PCs toward micro- and nanoscales.[3–7] As a result, various fabrication techniques have been investigated in the last decade, such as alternating layer deposition and etching,[8] and electron lithography in combination with dry etching.[9]

While most of the studies are concerned with utilizing the photonic band gaps, band edges, defect modes, and coupled cavity waveguides, the diversity of dispersion of photonic bands soon revealed a surprising feature: photonic crystals possess the ability to refract light as if they were a medium with a negative effective index of refraction. Proposed theoretically by Veselago in 1968,[10] the realization of negative refractive materials is presently under investigation, albeit by an intuitive approach to construct a medium with simultaneously negative permittivity (ϵ) and permeability (μ) values.[11–14] From this point of view, PCs opened a hidden door to completely novel and intriguing electromagnetic phenomena.

It is our aim in this article to present and discuss certain optical properties of PCs stemming from the presence of $n_{\text{eff}} < 0$ behavior. In particular, we demonstrate experimentally and numerically the negative refraction of EM waves by a photonic crystal slab. Two different mechanisms based on the band structure are discussed which generate $n_{\text{eff}} < 0$ medium. The negative refraction is achieved both for transverse electric (TE) and transverse magnetic (TM) polarizations using two different PCs, respectively. We then consider the focusing of EM waves emitted by an omnidirectional source to demonstrate that the PC-based lenses have superior properties compared to their conventional (positive refractive index) counterparts. In one case, the subwavelength resolution for the image is achieved, which cannot be obtained using lenses made of ubiquitous materials. In another case, we obtain far field focusing of the EM field through a PC slab, which does not depend on a certain optical axis, manifesting true flat lens behavior. Although these results are preliminary in the sense that their extension to three-dimensional PCs and towards optical frequencies is still ahead, they will certainly contribute from a fundamental physics point-of-view, and provide a basis for novel optical devices which have immaculate imaging capabilities and for other electromagnetic applications like antennas with novel properties. This article is organized as follows. In the second section, we investigate the negative refraction in a PC, utilizing its TM polarized

first band. The third section presents the focusing capabilities of the same PC, emphasizing the presence of subwavelength resolution at the image. In the fourth section, negative refraction analysis of another PC is presented, where this time, a TE polarized upper band is utilized. The fifth section extends the analysis for focusing properties of this PC structure and demonstrates the true flat lens behavior. We summarize the results in the Conclusion.

2. Negative Refraction of TM Polarized Electromagnetic Waves Through a Photonic Crystal Slab

The anomalous refraction behavior at a PC interface is first reported by Kosaka *et al.*, which was named the "super prism phenomenon."[15] Notomi studied the light propagation in strongly modulated PCs theoretically and established the connection between the effective refractive index and the band structure of the PC, by drawing analogies to the effective-mass approximation in electron-band theory.[16] Gralak *et al.*[17] reported on the anomalous refractive properties of photonic crystals. Luo *et al.*[18] investigated and proposed the conditions for all angle negative refraction through a photonic crystal and superlens phenomenon. Foteinopoulou *et al.*[19,20] demonstrated the negative refraction at the photonic crystal interface with negative refractive index using finite difference time domain (FDTD) simulations. Analysis of the band structures of PCs revealed the underlying mechanisms for the negative refraction: in one mechanism, the incident field couples to a band with convex equal-frequency contours (EFC) in **k**-space, where the conservation of the surface-parallel component of the wavevector, **k**, combined with the "negative" curvature of the band causes the incident beam bend negatively.[16,18] In this case, neither the group velocity nor the effective index is negative and the PC is essentially a positive index medium, exhibiting negative refraction. Alternatively, if the group velocity and phase velocity derived from the band dispersion are antiparallel for all values of **k**, the effective index of refraction of the PC becomes negative for that particular frequency range of the band.[19] Both mechanisms are confirmed experimentally.[21,22] In either case, however, the PC is locally a positive index medium, i.e. $\epsilon > 0$ and $\mu = 1$, which distinguishes them from left-handed composite metamaterials.[10–14]

In this section, we present the experimental and numerical investigation of negative refraction of TM polarized EM waves through a dielectric PC. The PC is a square array of cylindrical alumina rods with dielectric constant $\epsilon = 9.61$, a diameter of 3.15 mm, and length of 150 mm. The lattice constant is $a = 4.79$ mm. Propagation properties of the electromagnetic wave within the crystal can be described by studying EFCs in **k**-space. The TM polarized (i.e. electric field vector, **E**, is parallel to the rods) valence band of the photonic crystal calculated by plane wave expansion method, is shown in Fig. 1(a).

We follow the analysis of Ref. 18 to determine the negative refractive behavior from the band structure. Negative refraction requires convex EFCs for the PC, that are larger than the EFCs for air. The scaled frequency range that gives negative

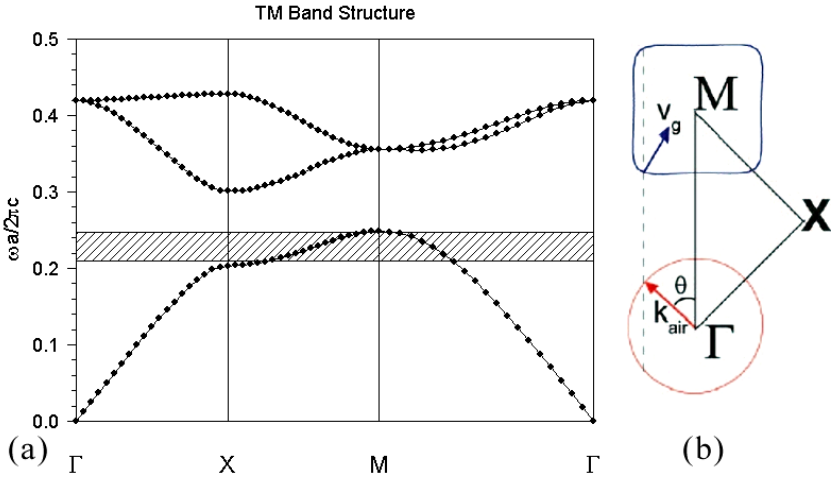

Fig. 1. (a) TM polarized band diagram of the 2D cubic photonic crystal. The frequency range in which negative refraction occurs extends from $\tilde{\omega} = 0.2093$ to $\tilde{\omega} = 0.2467$. (b) Frequency contours of air (*bottom*) and PC (*top*) at $\tilde{\omega} = 0.2189$. θ denotes the incidence angle from air to PC.

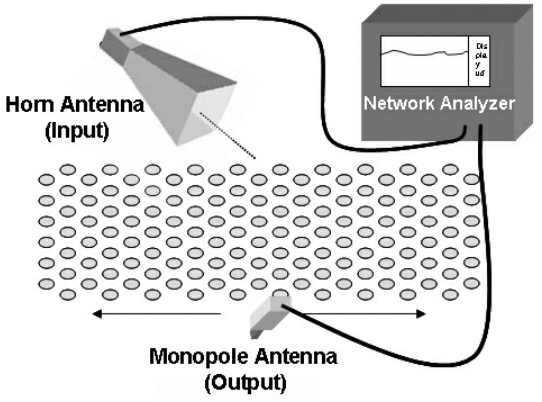

Fig. 2. Schematics of the experimental setup. In the refraction experiment, a transmitter horn antenna and a receiver monopole antenna are used. In the focusing effect experiment, both the transmitter and receiver are monopole antennas.

refraction for the present PC extends from $\tilde{\omega} = 0.2093$ to $\tilde{\omega} = 0.2467$. The EFCs for air and PC at $\tilde{\omega} = 0.2189$ are shown in Fig. 1(b). Note in the figure that conservation of surface-parallel wavevector gives the direction of the refracted waves inside the PC.

The negative refraction experiment setup consists of an HP 8510C network analyzer, a horn antenna as the transmitter and a monopole antenna as the receiver (Fig. 2). The incidence normal to interfaces extends along the GM direction of the PC. The incident waves make an angle of 45° to the normal of the GM interface.

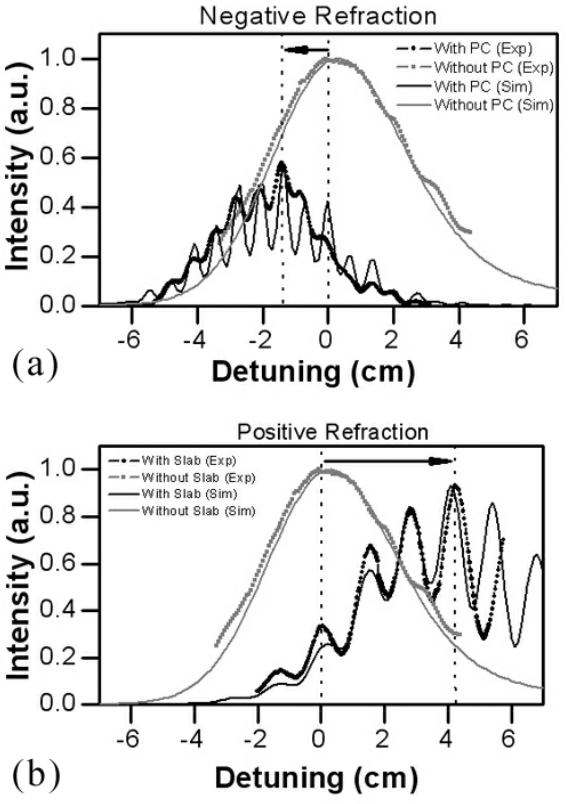

Fig. 3. (a) Refraction through the photonic crystal. Grey dots (*grey curve*) denote the measured (simulated) average intensity at the air–PC interface without PC. Black dots (*black curve*) denote the measured (simulated) power at the PC–air interface. (b) Same as in (a) but refraction through a crystal of polystryene pellets.

Operating frequency is selected as $\tilde{\omega} = 0.2189$. As explained later, the structure exhibits the maximum angular range of negative refraction at this frequency. The spatial distribution of the time averaged incident field intensity along the "front" (air-to-PC) and "back" (PC-to-air) interface locations are measured first in the absence of, and then by placing the PC. For a direct comparison of theoretical predictions and experimental results, simulation of the structure based on experimental parameters using a FDTD method is performed. Figure 3(a) summarizes the measured and simulated spatial distributions of intensity at the interfaces for the PC. The center-to-center shift of the outgoing beam relative to incident beam towards the left side clearly indicates the occurrence of negative refraction. For comparison, Fig. 3(b) shows the results for a slab that contains only polystyrene pellets, with a refractive index of 1.46. The refracted beam in this case appears on the right-hand side of the incident beam. The positive refractive index determined from the experiment is 1.52, which is close to the tabulated value of 1.46.

For the selected frequency, the incident field couples to the first band and propagates according to its dispersion. The advantage of the first band is that, since $\lambda > 2\sqrt{2}a$, the propagation does not suffer from Bragg reflections inside the PC and a well defined single beam propagates through the PC. Hence, Snell's law may be applied:

$$n_{\mathrm{PC}}(f, \mathbf{k}_i) \sin(\theta_r) = n_{\mathrm{air}} \sin(\theta_i)\,, \tag{1}$$

where θ_i is the angle of incidence, θ_r is the angle of refraction, and $n(f, \mathbf{k}_i)$ is the frequency dependent, anisotropic refractive index along the propagation direction $\mathbf{k}_i$. Based on Eq. (1), $n(f, \mathbf{k}_i)$ determined from the experiment is -1.94, which is very close to the theoretical value of -2.06 calculated by the FDTD method. It is also important to note that the 63% transmission at this frequency is almost 3 orders of magnitude larger than the typical transmission in a metallic left-handed material.[11,14]

In the aforementioned frequency range, the EFCs are square shaped around the **M** point in the Brillouin zone [Fig. 1(b)]. Figure 4 shows the resulting anisotropy of $n(f, \mathbf{k}_i)$ at $\tilde{\omega} = 0.2189$ ($f = 13.698$ GHz) that is determined for various angles of incidence. Negative refraction behavior is observed for the incidence angles larger than 20°. In this angular range $\mathbf{v}_g \cdot \mathbf{k}_{i\|} < 0$ (while $\mathbf{v}_g \cdot \mathbf{k}_i < 0$), where $\mathbf{v}_g$ is the group velocity inside the PC that is given by $\nabla_{\mathbf{k}}\omega(\mathbf{k})$. Here, $\mathbf{k}_{i\|}$ is a parallel component of the wavevector to the interface. At 13.698 GHz, the respective EFCs for air and for the PC have almost the same diameter which maximizes the angular range of negative refraction for this structure. If a higher frequency is used, the EFS for air will be larger than the EFS for the PC. In such a case, the maximum angle where we obtain negative refraction gets smaller due to total internal reflection. This results in a narrower angle range for the negative refraction behavior. If a lower frequency

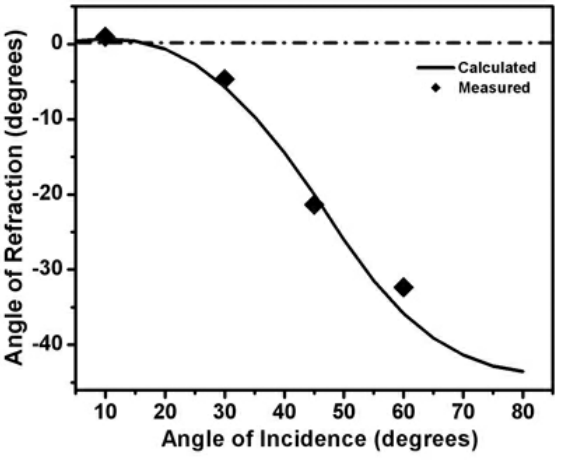

Fig. 4. Anisotropy of the effective index of refraction: Comparison of measured (*dots*) and simulated (*solid curve*) angles of refraction versus angles of incidence.

is used, we then have EFS for air that is smaller than the EFS for the PC. This in turn increases the minimum angle where we obtain negative refraction, which again reduces the angle range for the negative refraction behavior.

3. Focusing with Subwavelength Resolution through the 2D Photonic Crystal Slab

Superlensing, which is not limited by diffraction, was first proposed by Pendry,[23] as a negative refraction induced phenomenon, and has become a subject of intense debate.[24] Ideally this requires an isotropic index of refraction of negative unity and amplification of evanescent field modes while propagating across the lens structure which are required for an immaculate image formation on the focal plane. Anisotropy and deviations from negative unity will result in an impaired focusing, but still exhibit unusual focusing properties in contrast to positive refractive index materials. Cubukcu *et al.*[21] demonstrated experimentally the subwavelength resolution of a point source along a 2D PC–air interface. Later, Parimi *et al.*[22] obtained the near-field image formation of a point source using a 2D PC lens. The subwavelength imaging in PCs was recently studied in detail theoretically.[25]

To investigate the focusing ability of the present PC, a slab having 15 layers in the propagation direction and 21 layers in the lateral direction is used. The operation frequency is set to 13.698 GHz, having the largest angular range for negative refraction. FDTD simulations with experimental parameters predict the formation of an image 0.7 mm away from the PC–air interface for a point source that is placed 0.7 mm away from the air–PC interface. We first simulated the distribution of time-averaged intensity along the PC–air interface with and without the PC (solid curve and thin dotted curve in Fig. 5). In the experiment, a monopole antenna is

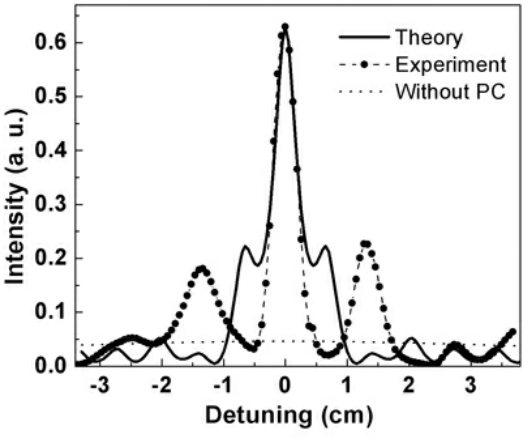

Fig. 5. Focusing: measured power distribution (*dots*) and calculated average intensity (*solid curve*) at the image plane. Full width at half maximum of the measured image is $\approx 0.21\lambda$. Spatial power distribution without PC is also shown (*dotted thin line*).

used as the point source. The measured power distribution along the interface is depicted by large black dots in Fig. 5. The full width at half maximum (FWHM) of the measured focused beam is found to be 0.21λ, which is in good agreement with the calculated FWHM. In contrast, the calculated FWHM of the beam at this plane in the absence of the PC is found to be 5.94λ. This implies an enhancement of the transmitted field about $25\times$ compared to free space. We stress the point that the narrow incidence angle range for negative refraction ($< 20°$), and the anisotropy restricts the position of the source in the vicinity of the crystal surface for proper observation of focusing effect. According to a recent theoretical study by Luo *et al.*,[25] the subwavelength imaging is possible due to the amplification of evanescent waves through the photonic crystal. They have also found that the periodicity of the photonic crystal imposes an upper cutoff to the transverse wavevector that can be amplified, which brings an ultimate limit to the superlens resolution. Within this description, we can also introduce an upper limit on the location of the source from the PC. As the evanescent waves have to reach the surface of the PC (before they decay away), the source has to be close enough to the PC. In this sense, the theoretically predicted and the experimentally observed subwavelength resolution in PCs will be limited to the cases where the source is close to the PC.

For a more elaborate investigation of the presence of subwavelength resolution, we use the same PC structure and introduce two coherent point sources which are separated by a distance of $\approx \lambda/3$ and placed 0.7 mm away from the air–PC interface. Figure 6(a) shows the lateral profile of the transmitted power 0.7 mm away from the PC–air interface. The agreement between the simulated and measured data is evident. When the crystal is removed, no features are visible on the power profile (*dashed line*). To exclude interference effects due to coherence, we repeat the experiment using two incoherent point sources having frequencies 13.698 GHz and 13.608 GHz, respectively. Independent signal generators are used for driving the monopole antennas to ensure incoherent behavior, and a powermeter is used for measurement. The measured and simulated power distribution in the presence of photonic crystal 0.7 mm away from the second interface is shown in Fig. 6(b). Again, the peaks corresponding to the incoherent source pair are clearly resolved.

One can argue that the observed enhanced resolution can be attributed to the high refractive index as in the case of oil (or solid) immersion microscopy. In this case, higher wavevectors which are evanescent in air can transmit through the crystal and form a near-field image with subwavelength resolution. In order to check this possibility, the incoherent source setup was simulated for a uniform dielectric slab with a high refractive index. The dashed and dash-dotted lines in Fig. 6(b) indicate the power distribution in the presence of a dielectric slab of $n = 3.1$ and $n = 15$, respectively. Note that $n = 3.1$ is also the refractive index of the alumina rods used in constructing the photonic crystal. Even with the use of artificially high refractive index ($n = 15$), the sources are not resolved. Besides, the large reflection due to high index contrast at the interface significantly reduces the transmitted power when compared to the high (63%) transmission obtained from the photonic crystal

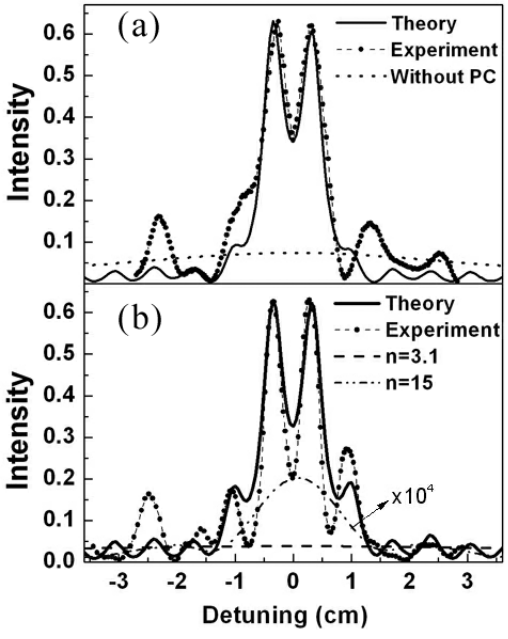

Fig. 6. (a) Measured (*dots*) and simulated (*solid curve*) power distribution at 0.7 mm away from the PC–air interface for two coherent sources separated by $\approx \lambda/3$ at 0.7 mm away from the air–PC interface. The dotted line denotes the simulated intensity profile in the absence of PC. (b) Same setup with two incoherent point sources. The lower dashed and dot-dashed curves indicate the power distribution for uniform dielectric slabs with refractive indices $n = 3.1$ and $n = 15$, respectively. Note the magnification of the $n = 15$ curve.

at this operating frequency. So, even if the observed subwavelength is associated with near-field effects, this is not achievable by ubiquitous materials.

4. Spectral Negative Refraction Analysis of the TE Polarized Band of a 2D Photonic Crystal

In Sec. 2, the negative refraction originating from the convex equal frequency contours (EFC) of the first band around the M-point in **k**-space is investigated. The first band has a partial gap around Γ-point, and the EM waves are forced to move along the ΓM direction, where the conservation of the surface-parallel component of the wavevector causes negative refraction (Fig 1(b)). Although the focusing abilities surpasses that of conventional lenses as demonstrated in Sec. 3, both the frequency range and the angular range for the occurrence of negative refraction is limited. In this section, we employ a different band topology of a 2D photonic crystal to obtain negative refraction. Our aim is to achieve a negative n_{eff} with higher isotropy. Based on the analysis presented in Ref. 19, we utilize a TE polarized upper band of the PC (i.e. the magnetic field **H** is parallel to the dielectric rods). A similar study using TM polarized band was reported by Martinez *et al.*[27] Recently, the negative refraction and focusing studies have been extended to infrared frequencies.[28]

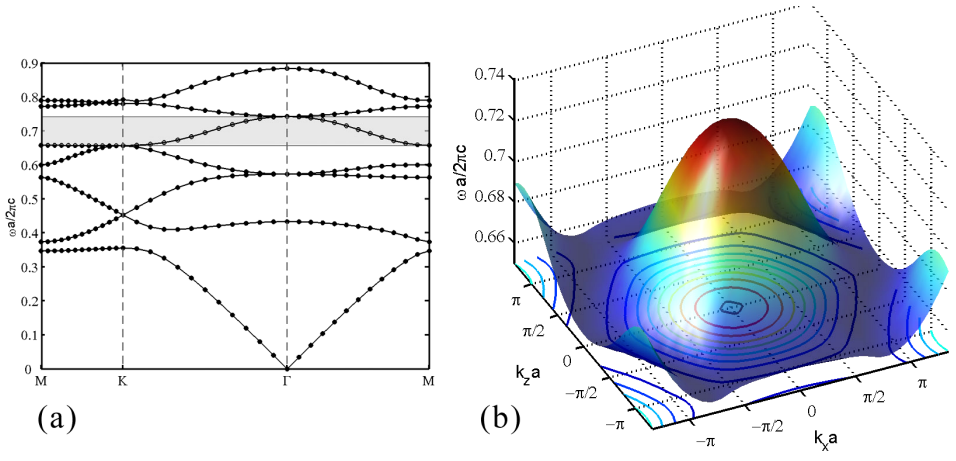

Fig. 7. (a) TE polarized band structure of the hexagonal PC. The 5th band (*shaded*) has negative effective index of refraction. (b) The surface (*transparent shell*) of the 5th band in the full Brillouin zone. Some equal-frequency contours are projected to the Brillouin zone plane.

The PC is a hexagonal lattice of alumina rods in air with a lattice period of $a = 4.79$ mm. The rods have dielectric constant $\epsilon = 9.61$, diameter $2r = 3.15$ mm, and length $l = 150$ mm. Figure 7(a) shows the TE polarized band structure in the first Brillouin zone. The 5th band shaded in the figure extends from $\tilde{f} = 0.65$ ($f = 40.65$ GHz) to $\tilde{f} = 0.74$ ($f = 46.27$ GHz), where $\tilde{f} = fa/c$ is the scaled frequency. In Fig. 7(b), the band surface in the full Brilloin zone along with the projected EFCs are shown. The EFCs of the band are shrinking with increasing frequency, contrary to the EFCs in air ($n = 1$) which are given by the dispersion $\omega = ck$. As a result, the effective refractive index $n_p = \text{sgn}(\mathbf{v}_g \cdot \mathbf{k}_f)(c|\mathbf{k}_f|/\omega)$, becomes negative due to sign of the antiparallel group velocity, $\mathbf{v}_g = \nabla_{\mathbf{k}}\omega$ and the phase velocity $\mathbf{v}_p = (c/|n_p|)\hat{k}_f$. Here c is the speed of light in vacuum, and $\hat{k}_f$ is the unit wavevector in the PC. We note that the EFC starts to deviate from the circular shape towards the bottom edge of the band, which will induce some anisotropy. We will discuss this effect later.

The refraction spectra are measured by a setup consisting of an HP 8510C network analyzer, a microwave horn antenna as the transmitter and a waveguide antenna as the receiver. Figure 8 displays the schematic view of the setup. The PC has 7 layers along the incidence (GM) direction and 31 layers along the lateral direction. The horn antenna is on the negative side of the PC with respect to its central axis. The spatial intensity distribution along the PC–air interface is scanned by $\Delta x \sim 1.27$ mm steps, while the frequency is swept from 38.5 GHz to 43.5 GHz in 400 steps, averaged over 256 measurements at each frequency.

Figure 9(a) displays the transmission spectra as a function of frequency and lateral position for three different incidence angles of $\theta_i = 15°$, $30°$, and $45°$. It is evident from the figure that the transmitted beam appears on the negative side.

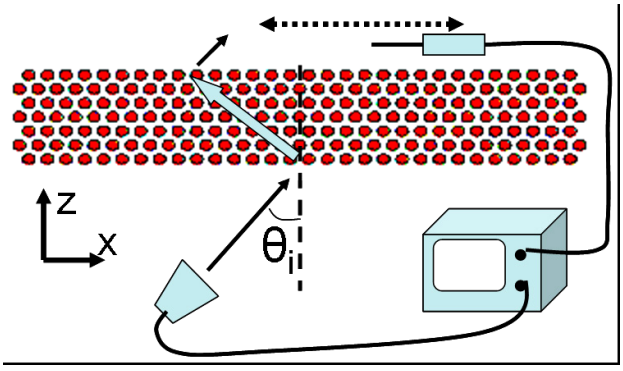

Fig. 8. Schematic of the refraction spectra measurement setup. The EM wave is emitted from a horn antenna, incident to the PC at angle θ_i. The lateral intensity distribution of the refracted beam at the other interface is scanned by a monopole antenna. An HP 8510C network analyzer is used to obtain the transmission spectra.

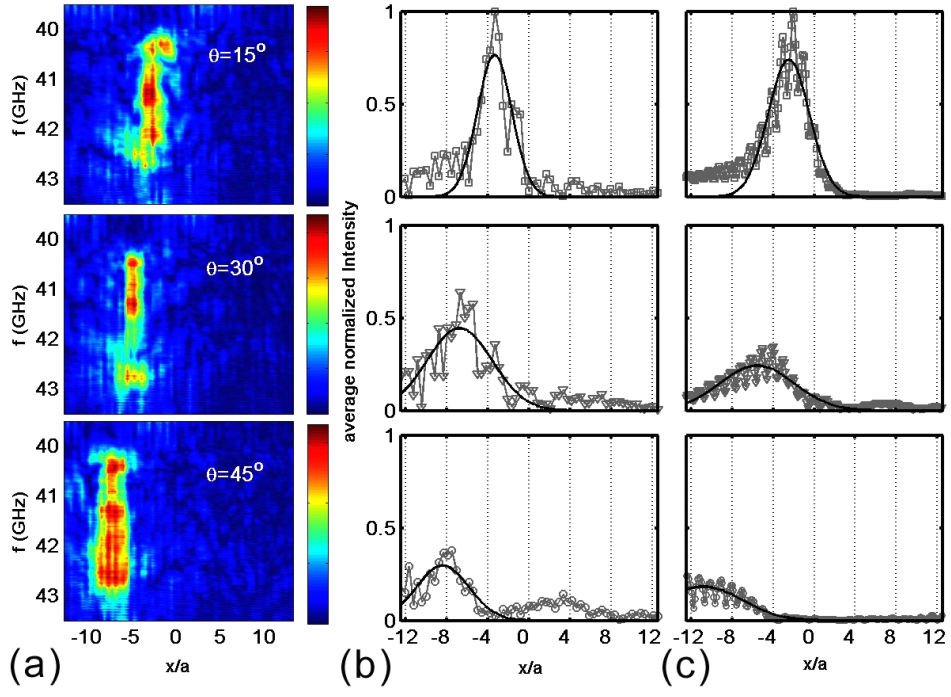

Fig. 9. (a) Measured negative refraction spectra of the 5th band along the PC–air interface for incidence angles $\theta_i = 15°, 30°$ and $45°$. Measured (b) and simulated (c) intensity profiles at $f = 41.7$ GHz for the respective incidence angles. Solid curves indicate Gaussian fits.

When the incidence angle is increased, the transmission shifts towards left accordingly. To investigate the beam profiles, the spatial cross section and corresponding FDTD simulations at $f = 41.7$ GHz [$\tilde{f} = 0.667$ are plotted in Fig. 9(b) and Fig. 9(c),

respectively]. We note that the incident field has a Gaussian beam profile centered at $x = 0$ (not shown on figures). The intensities are normalized with respect to the maximum intensity for the 15° incidence. The lateral shift is accompanied by a decrease in the transmission intensity. This is mainly due to the increase of reflection with increasing incidence angle. Another contribution is the diffraction induced out-of-plane (y-direction) loss within the PC.

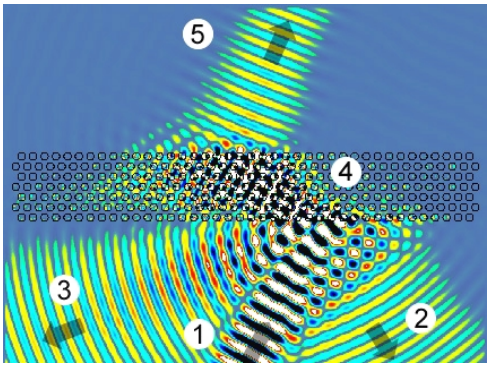

Fig. 10. Simulated negative refraction of a plane wave at $f = 41.7$ GHz incident at $\theta = 30°$ to the PC interface (*mark 1*). Zero order (*mark 2*) and higher order (*mark 3*) reflections occur. The refracted (*mark 4*) the transmitted (*mark 5*) components propagate as single beams.

Before we commence, an effective index of refraction calculation using the measured and simulated refraction data, visualizing the field distribution by an FDTD simulation, may help to gain insight about the presence/absence of higher order reflected and refracted wave components. Figure 10 depicts a simulation for the $\theta_i = 30°$ incidence. Evidently, higher order reflection (*mark 3*) is present because at $\tilde{f} = 0.667$, the condition $\tilde{f} \leq a/(2a_{\text{int}})$ is not met where a_{int} is the interface period of the PC.[18,26] The refracted beam, however, appears to be a single component, which is also suggested by the single transmitted component on the other side of the PC. One may argue that the simulation at $\theta_i = 30°$ is not conclusive as the surface parallel wavevector changes with incidence angle. This is indeed the case, but the simulations of the present structure indicate that a single refracted beam is present for incidence angles $\theta_i \leq 45°$. Several theoretical studies pointed out that single beam refraction at higher bands is possible.[16,20,26] We therefore assume that most of the propagating power is coupled to the zero-order diffracted wave, and employ Snell's law given by Eq. (1). For $\theta_i = 15°, 30°$, and 45° we obtain $n_{\text{eff}} = -0.52, -0.66$, and -0.86 from the experiment data, and $n_{\text{eff}} = -0.66, -0.72$, and -0.80, from the FDTD simulations.

In general, n_{eff} depends both on the parallel component of the wavevector (i.e. the angle of incidence) and the frequency of the field: $n_{\text{eff}}(\mathbf{k}_i, \omega)$. The refraction spectra in Fig. 9(a) exhibits both dependencies to a certain extent. The **k**-dependent anisotropy is apparent from the numerical values of n_{eff} obtained by applying Snell's

Law. The frequency 41.7 GHz for which the lateral beam profiles are plotted is rather close to the lower edge of the band, which makes this anisotropy more prominent. As mentioned, increasing the parallel component of the wavevector may also induce higher order reflection and refraction at the interface. We stress that the frequency range (40.65–43 GHz) plotted in Fig. 9(a) covers only the lower half of the band. The range above 43 GHz was beyond the operation limit of our measurement setup. The frequency dependent anisotropy occurring in this frequency range is not sufficient to reflect itself in the displayed spectra. Obviously, n_{eff} of the band should change with frequency since it should approach to zero at the upper band edge. Overall, the band manages to provide a negative refracted uniform beam within the measured frequency range.

5. Focusing Properties and the True Flat Lens Behavior of the Photonic Crystal

Similar to the analysis given in Sec. 3, we now investigate any focusing property of the PC in this frequency range. For the present PC, we first performed FDTD simulations for a TE polarized point source at $f = 42.07$ GHz located at a distance $d_{\text{src}} = 2\lambda$ away from air–PC interface. Figure 11(b) shows the resulting spatial intensity distribution in the image plane, normalized by the maximum intensity value. The PC–air interface is located at $z = 0$. The peak indicates focusing behavior unambiguously (we also refer the reader to Fig. 13 for the simulated 2D **H**-field map, where the convergence of the wavefronts along the optical axis is clearly visible). We would like to emphasize that the focusing occurs away from the PC–air interface, observed at $z \approx 8\lambda$. Therefore, unlike the focusing discussed in Sec. 3, this PC does not perform "imaging" in the strict sense. Also a subwavelength resolution as presented in Fig. 5 may not be present. Focusing far from the interface however, excludes channeling induced focusing effects, which occur close to the interface.[29]

In the experiment, we employed a waveguide aperture as the source, which, due to the diffraction at the aperture, provides sufficiently omnidirectional radiation to imitate a TE polarized monopole antenna. On the other hand, the intensity distribution in the focusing plane is measured by a monopole antenna for better spatial resolution. For $d_{\text{src}} = 2\lambda$, the propagation direction z is first scanned for locating the maximum intensity, and then, lateral cross sections of intensity at several z around the peak position are measured. In Fig. 11(a), the focusing of the beam both in lateral and longitudinal directions is evident. The maximum intensity (normalized to unity) is observed at $d_{\text{focus}} \approx 8\lambda$. The longitudinal extend of the focusing indicates that n_{eff} deviates from negative unity, and bears a certain amount of anisotropy. We stress that even when n_{eff} were perfectly isotropic and uniform, a value different from -1 would not generate point focusing and would induce an aberration of the image.

The flat lens behavior of the PC structures was emphasized in recent studies.[22] In this case, the focusing properties are preserved at an arbitrary lateral location

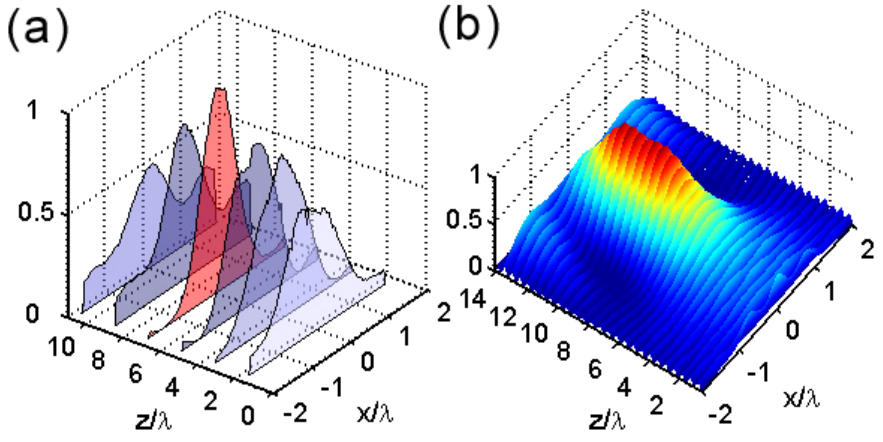

Fig. 11. (a) Lateral intensity profiles measured at six different positions along the propagation direction: $z/\lambda = 1.78, 3.56, 5.34, 7.12, 8.90$ and 10.68. $z = 0$ corresponds to the PC interface. Source is located at $z/\lambda = 2$ away from the other interface (not shown in figure). (b) The corresponding FDTD-simulated 2D magnetic field intensity in the image plane.

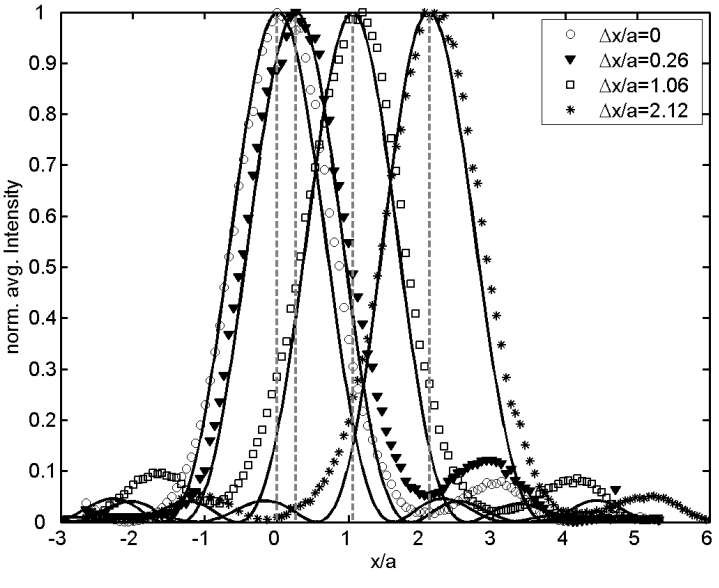

Fig. 12. The measured (*symbols*) and simulated (*solid curves*) lateral intensity profiles at the focal distance ($z/\lambda \approx 8$) for different lateral shifts. The respective source locations are denoted by vertical dashed lines.

of the source along the interface. To demonstrate this, we have shifted the source laterally and measured the lateral beam profile at the focal point. In Fig. 12, the source positions (*vertical dashed lines*) and the peak positions of the focused beam (*symbols*) are in excellent agreement. The agreement is supported by the simulated

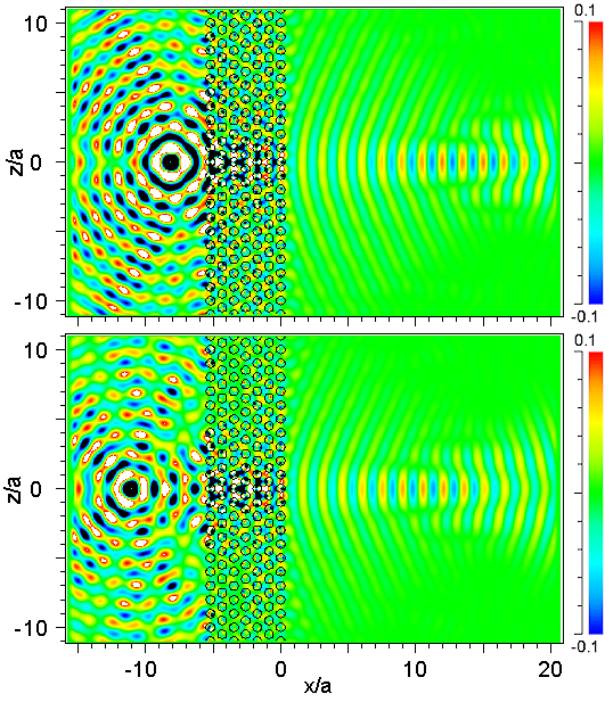

Fig. 13. The FDTD simulation of the 2D magnetic field distribution $H(x, z)$ for $d_{\text{src}} = 2\lambda$ (*top*) and $d_{\text{src}} = 4\lambda$ (*bottom*).

profiles (*solid curves*) using a true point source. The average FWHM of the profiles at $d_{\text{focus}} \approx 8\lambda$ depicted in Fig. 12 is $1.60a \approx 1.08\lambda$, on par with the wavelength. As mentioned at the beginning of this section, a subwavelength focusing as discussed in recent studies[21,25] is not concerned here. The subwavelength focusing requires the amplification of evanescent waves through the photonic crystal for image formation. This implies an upper limit on the location of the source and image from the PC, since the evanescent waves decay rapidly away from the interfaces.

We further investigated the effect of shifting the source towards and away from the PC interface. The FDTD-simulated 2D map of the magnetic field, $H(x, z)$, plotted in Fig. 13 shows that when the source is moved from $d_{\text{src}} = 2\lambda$ to $d_{\text{src}} = 4\lambda$ away, the focus pattern on the other side shifts accordingly towards the PC–air interface. In Fig. 14, the measured lateral profiles at focus points for various d_{src} are plotted. From the determined focal positions we have found that $(d_{\text{src}} + d_{\text{focus}})$ remains roughly constant, which may be investigated further within a geometric optics analysis. The figure also displays the intensity profile in the absence of the PC for $d_{\text{src}} = 2\lambda$ case (*dotted line*) which shows almost no features about the source location. Overall, the focused beam by the PC is 12 dB higher relative to freespace propagation at the focal distance and has a FWHM of the order of λ.

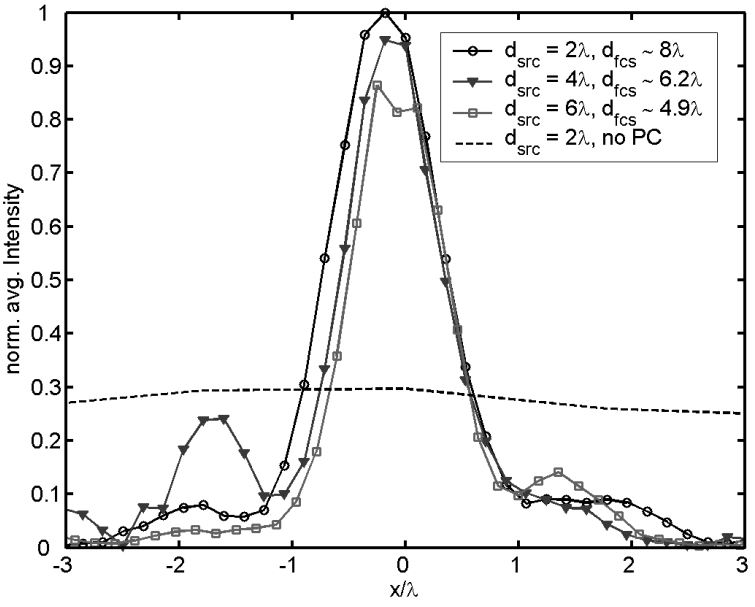

Fig. 14. The measured lateral intensity profiles at respective focal distances for different source distances. The intensity is normalized by the $d_{\mathrm{src}} = 2\lambda$ profile peak. The dashed line denotes the intensity profile in the absence of PC for $d_{\mathrm{src}} = 2\lambda$.

6. Conclusion

In this article, the negative refraction and the focusing abilities of 2D dielectric photonic crystals are investigated. We have seen that an effective index of refraction, n_{eff}, can be defined from the band structure of the PC, which, under convex EFCs, can take negative values and can be associated with refraction of electromagnetic waves through the PC. The isotropy and spectral range of n_{eff} depend on the details of the band structure. The focusing abilities associated with n_{eff} is demonstrated to be promising: both the subwavelength resolution and far field focusing are achievable using PC with appropriate band structures. Moreover, a simple rectangular PC slab can exhibit true flat lens behavior (i.e. absence of an optical axis) which makes it very simple and robust both from fabrication and application points of view.

We would like to emphasize that the electromagnetic phenomena reported in this article depend only on the refractive index of the dielectric material and on the geometrical parameters of the 2D PC, hence it should be scalable across the electromagnetic spectrum. With advancing fabrication techniques, photonic crystals are now envisaged as essential building blocks of applications in the infrared and optical frequencies.

References

1. J. D. Joannopoulos, R. D. Meade and J. N. Winn, *Photonic Crystals: Molding the Flow of Light* (Princeton University Press, Princeton, 1995).
2. C. M. Soukoulis (ed.), *Photonic Crystals and Light Localization in the 21st Century* (Kluwer, Dortrecht, 2000).
3. H. Benisty, C. Weisbuch, D. Labilloy, M. Rattier, C. J. M. Smith, T. F. Krauss, R. M. De La Rue, R. Houdré, U. Oesterle, C. Jouanin and D. Cassagne, *J. Lightwave Technol.* **17** (1999) 2063.
4. T. Krauss, Y. P. Song, S. Thomson, C. D. Wilkinson and R. M. De La Rue, *Electron. Lett.* **30** (1994) 1444.
5. P. L. Gourley, J. R. Wendt, G. A. Vawter, T. M. Brennan and B. E. Hammons, *Appl. Phys. Lett.* **64** (1994) 687.
6. S. Noda, M. Imada, S. Ogawa, M. Mochizuki and A. Chutinan, *IEEE J. Quantum Electron.* **38** (2002) 726.
7. J. M. Lourtioz, H. Benisty, A. Chelnokov, S. David and S. Olivier, *Ann. Telecommun.* **58** (2003) 1197.
8. E. Kuramochi, M. Notomi, T. Kawashima, C. Takahashi, J. Takahashi, T. Tamamura and S. Kawakami, *Int. Workshop of Photonic and Electronmagnetic Crystal Structures (PECS II)*, March 2000, Sendai, Japan.
9. Y. Sugimoto, N. Ikeda, N. Carlsson, K. Asakawa, N. Kawai and K. Inoue, *J. Appl. Phys.* **91** (2002) 922.
10. V. G. Veselago, *Sov. Phys. Usp.* **10** (1968) 509.
11. D. R. Smith, W. J. Padilla, D. C. Vier, S. C. Nemat-Nasser and S. Schultz, *Phys. Rev. Lett.* **84** (2000) 4184.
12. R. A. Shelby, D. R. Smith, S. C. Nemat-Nasser and S. Schultz, *Appl. Phys. Lett.* **78** (2001) 481.
13. R. A. Shelby, D. R. Smith and S. Schultz, *Science* **292** (2001) 77.
14. M. Bayindir, K. Aydin, E. Ozbay, P. Markos and C. M. Soukoulis, *Appl. Phys. Lett.* **81** (2002) 120.
15. H. Kosaka, T. Kawashima, A. Tomita, M. Notomi, T. Tamamura, T. Sato and S. Kawakami, *Phys. Rev.* **B58** (1998) R10096.
16. M. Notomi, *Phys. Rev.* **B62** (2000) 10696.
17. B. Gralak, S. Enoch and G. Tayeb, *J. Opt. Soc. Am.* **A17** (2000) 1012.
18. C. Luo, S. G. Johnson, J. D. Joannopoulos and J. B. Pendry, *Phys. Rev.* **B65** (2002) R201104.
19. S. Foteinopoulou, E. N. Economou and C. M. Soukoulis, *Phys. Rev. Lett.* **90** (2003) 107402.
20. S. Foteinopoulou and C. M. Soukoulis, *Phys. Rev.* **B67** (2003) 235107.
21. E. Cubukcu, K. Aydin, E. Ozbay, S. Foteinopoulou and C. M. Soukoulis, *Nature* **423** (2003) 604; *ibid. Phys. Rev. Lett.* **91** (2003) 207401.
22. P. V. Parimi, T. W. Lu, P. Vodo and S. Sridhar, *Nature* **426** (2003) 404.
23. J. B. Pendry, *Phys. Rev. Lett.* **85** (2000) 3966.
24. R. W. Ziolkowski and E. Heynman, *Phys. Rev.* **E64** (2001) 056625.
25. C. Luo, S. G. Johnson, J. D. Joannopoulos and J. B. Pendry, *Phys. Rev.* **B68** (2003) 045115.
26. S. Foteinopoulou and C. M. Soukoulis, arxiv.org: cond-mat/0403542 (2004), submitted to *Phys. Rev.* **B**.
27. A. Martínez, H. Míguez, A. Griol and J. Martí, *Phys. Rev.* **B69** (2004) 165119.
28. A. Berrier, M. Mullot, M. Swillo, M. Qiu, L. Thylén, A. Talneau and S. Anand, *Phys. Rev. Lett.* **93** (2004) 073902.
29. Z.-Y. Li and L.-L. Lin, *Phys. Rev.* **B68** (2003) 245110.